Journal of Alloys and Compounds 787 (2019) 794–800

Contents lists available at ScienceDirect

Journal of Alloys and Compounds

journal homepage: http://www.elsevier.com/locate/jalcom

Tuning of the magnetic properties of $Hf_2Co_{11}B$ alloys through a combined high pressure torsion and annealing treatment

A. Musiał [a, *], Z. Śniadecki [a], N. Pierunek [a], Yu. Ivanisenko [b], D. Wang [b, c], M.H. Fawey [b, d], B. Idzikowski [a]

[a] Institute of Molecular Physics, Polish Academy of Sciences, M. Smoluchowskiego 17, 60-179, Poznań, Poland
[b] Institute of Nanotechnology, Karlsruhe Institute of Technology, Hermann-von-Helmholtz-Platz 1, D-76344, Eggenstein-Leopoldshafen, Germany
[c] Karlsruhe Nano Micro Facility (KNMF), Karlsruhe Institute of Technology, Hermann-von-Helmholtz-Platz 1, D-76344, Eggenstein-Leopoldshafen, Germany
[d] Joint Research Laboratory Nanomaterials (KIT and TUD) at Technische Universität Darmstadt (TUD), Jovanka-Bontschits-Str. 2, D-64287, Darmstadt, Germany

ARTICLE INFO

Article history:
Received 31 October 2018
Received in revised form
7 February 2019
Accepted 8 February 2019
Available online 10 February 2019

Keywords:
Intermetallics
Magnetic properties
Plastic deformation
Magnetocrystalline anisotropy
Microstructures
Melt-spinning

ABSTRACT

The evolution of crystalline structure induced by heat treatment and high pressure torsion (HPT) deformation and its influence on the magnetic properties of amorphous and partially crystalline $Hf_2Co_{11}B$ ribbons were investigated. Slight improvement in thermal stability of the as-quenched sample after deformation was observed as indicated by the shift of the first crystallization peak from 592 to 598 °C. Plastic deformation of the initially annealed partially crystalline alloy led to its amorphization, as confirmed by X-ray diffraction (XRD). However, the presence of small volume fraction of needle-like nanocrystals was indicated by transmission electron microscopy (TEM). The annealed sample subjected to high pressure torsion was characterized by the reduced coercive field, from 0.7 to 0.2 kOe, while the subsequent reannealing of the deformed sample enhanced the coercivity up to 1.3 kOe. Transmission electron microscopy analysis revealed the existence of nanocrystals with large lattice constant of 8 Å characteristic of Hf_2Co_{11} phase. Magnetic measurements also confirmed that some nanocrystals of the hard magnetic phase were present in the sample after deformation, indicating their importance for maximization of coercivity. The isolation of this quite elusive phase is clearly linked to magnetic performance and the method combining severe plastic deformation (SPD) and heat treatment was found to allow tuning of the structure and improving the hard magnetic properties.

1. Introduction

Nd-Fe-B compounds are widely used in the industry because of their high energy product $|BH|_{max}$. Small amounts of Dy or Tb are substituted in place of Nd atoms to optimize coercivity and additionally to slightly increase the Curie temperature (T_C). Rare-earth materials play an increasingly important role in global manufacturing, but simultaneously they should be treated as critical due to the impact of possible supply disruptions. It has prompted efforts to reduce their usage in the magnetic materials industry. There are many ongoing investigations aiming to find new materials without rare-earth elements for permanent magnet applications. The enhancement of magnetic properties can be achieved, for example, by microstructure optimization and/or by partial substitution of nominal composition [1]. The newly invented alloy should consist of more available elements than rare-earths and show high Curie temperature and high value of $|BH|_{max}$. There are just a few groups of compounds such as Mn-Al/Bi [2,3] or Zr-Co [4], that have been considered as candidates for replacement of some permanent magnet materials used nowadays. The energy product of these compounds has not been high enough to replace rare-earth permanent magnets up to date. They can be still useful in industrial applications on condition that their microstructure is optimized by the refinement of grains, like in the case of soft magnetic alloys [5,6]. It can be achieved by different methods like mechanical milling [7], grinding [8], variation of the nominal composition [9], sintering [10] or a combination of several of these approaches [11]. It is well known that the severe plastic deformation (SPD) leads to a significant decrease in grain size [12,13]. Microstructure can be also optimized by SPD triggered phase

* Corresponding author.
E-mail address: musial@ifmpan.poznan.pl (A. Musiał).

https://doi.org/10.1016/j.jallcom.2019.02.098
0925-8388/

transition [14]. One of the SPD techniques, high pressure torsion (HPT), can also lead to amorphization of the crystalline compounds [15] or crystallization of the amorphous precursors [16], depending on the particular system and its properties.

Hf-Co alloys can be synthesized in the amorphous state using rapid quenching [17]. Subsequent isothermal annealing leads to crystallization of the hard magnetic phase. The crystalline structure of the hard magnetic phase is still under debate and is considered to be $HfCo_7$ [18] or 2:11 phase (reported for Zr_2Co_{11} [19] and $Hf_2Co_{11}B$ alloys [20]). We have already reported that for the Hf-Co-B system, the Hf_2Co_{11} phase can exist in two similar structures, rhombohedral and orthorhombic [21].

In the present paper we focus on the tunability of magnetic properties and possibility to improve the hard magnetic properties of $Hf_2Co_{11}B$ alloy by a combined treatment of high pressure torsion and isothermal annealing. Besides, the influence of HPT process on the structural and magnetic properties of $Hf_2Co_{11}B$ alloy in two initial states (as-quenched and isothermally annealed) is deduced.

2. Experimental details

High purity Hf, Co, and B (3 N or more) were used to prepare the master alloy with the nominal composition of $Hf_2Co_{11}B$ by arc-melting in the argon atmosphere. Elements were remelted several times to ensure homogeneity. Subsequently, inductively melted sample was rapidly quenched by melt-spinning on a copper wheel rotating with the linear surface velocity of 30 ms^{-1}. The thickness of synthesized ribbon was equal to 30 ± 5 μm. Structural data were obtained by X-ray diffraction (XRD) with the use of TUR-M62 diffractometer (HZG4 goniometer) with CoK_α radiation ($\lambda = 1.7889$ Å) in Bragg-Brentano geometry. The crystallization process of the as-quenched sample was investigated by differential scanning calorimetry (DSC) with heating rate $q = 20$ $Kmin^{-1}$, between 100 and 800 °C, using Netzsch DSC 404 apparatus. Magnetic hysteresis loops were measured by vibrating sample magnetometer option in Quantum Design Physical Property Measurement System. For plastic deformation experiments, all the ribbons were cut in pieces of around 1 cm in length and stacked, to form disks of 10 mm in diameter constrained by the shape of anvils, after HPT process. The HPT was performed under quasi-hydrostatic pressure of 6 GPa at room temperature on the sample with 10 mm in diameter, placed between two flat anvils. TEM lamellae from the as-quenched sample and the annealed and HPT processed sample were prepared using Focused Ion Beam (FIB) system (FEI Strata 400 STEM) equipped with an OmniProbe 200 micromanipulator for in-situ lift-out. The preparation was initially performed at 30 kV with an ion beam current of 21 nA. The lamellae were thinned to about 60 nm thickness using ion beam currents from 0.44 nA down to 26 pA. The final thinning step was performed at 5 kV with 15 pA ion beam current. High resolution transmission electron microscopy (HRTEM) and selected area electron diffraction (SAED) data were acquired in a FEI Titan 80–300 microscope with image spherical aberration corrector and operated at an accelerating voltage of 300 kV.

3. Results and discussion

Two samples in different initial states were subjected to high pressure torsion. The first one ($S_{as\text{-}q}$) was amorphous in the as-quenched state and the second one (S_A) was partially crystalline (annealed from the fully amorphous one at $T_a = 570$ °C for $\tau_a = 60$ min). During the HPT process the stacks of as-quenched or annealed ribbons were deformed at a rotation speed of 1 rpm with various sequences of rotations N: N = 0.5 + 0.5 + 1 for the as-quenched and N = 0.5 + 0.25 for the annealed ribbons. Deformed samples are denoted as $S_{as\text{-}q\_H}$ and S_{AH}, respectively. Sample S_{AH} was subsequently annealed for the second time in the same conditions as in the previous step of the synthesis ($T_a = 570$ °C, $\tau_a = 60$ min) and is denoted as S_{AHA}.

X-ray diffraction patterns of samples in as-quenched state and after HPT are shown in Fig. 1. No changes are visible after deformation and the fully amorphous structure is preserved. The Scherrer formula [22] was used to calculate sizes of coherently scattered domains L. For $S_{as\text{-}q}$ L is equal to 14.2 Å, and almost the same value $L = 14.1$ Å was obtained after HPT. These results are in accordance to those reported in our previous paper [21]. The shortest interatomic distances R were determined by the Ehrenfest equation [22] to be equal to 2.58 Å for both samples. This value is close to 2.6 Å, which was determined for the ternary RE–Co–B amorphous alloys with RE = Y, Tb and Ho [23].

Differential scanning calorimetry results are depicted in Fig. 2. Crystallization processes in both samples are very similar and consist of three crystallization steps without any evidence of glass transition, similarly to Zr-Co-B compounds [24]. This may be due small energy difference between undercooled glassy state and internally equilibrated state after structural relaxation. Glass transition is a kinetic phenomenon and the cooling rate of melt-spinning is decisive in the equilibration process. Therefore, manifold iso configurational states can be obtained, which results in different enthalpies of relaxation process. In comparison to as-quenched sample, the ribbon subjected to HPT reveals slightly improved thermal stability, evidenced by higher temperature corresponding to the maximum of the first crystallization peak (T_{p1}). For $S_{as\text{-}q}$ sample T_{p1} is equal to 592 °C, while it reaches 598 °C for the deformed sample. The temperatures corresponding to the onset of crystallization event in $S_{as\text{-}q}$ and $S_{as\text{-}q\_H}$ samples are equal to 577 and 579 °C, respectively. The maxima of the third crystallization peak are nearly the same ($T_{p3} = 650$ and 651 °C for the as-quenched and deformed alloys, respectively). Increased crystallization temperature can be connected with the influence of external compressive stress during high pressure torsion application. Such behavior has been observed by *in-situ* resistivity measurements in thin films subjected to uniaxial extrinsic stress [25] and explained by the influence of stress on the cavities and the interactions between atoms. Even slight changes in local atomic configurations could limit the mobility of atoms and consequently increase thermal stability of the system.

Magnetic hysteresis loops $M(H)$ for $Hf_2Co_{11}B$ in as-quenched state and after HPT were collected at room temperature and are shown in Fig. 3. Density of the alloy was assumed on the basis of

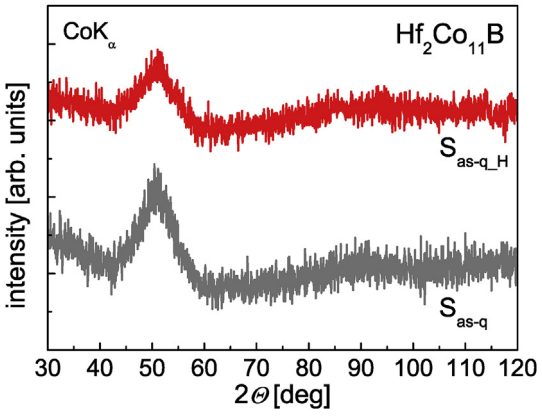

Fig. 1. X-ray diffraction (XRD) patterns of $Hf_2Co_{11}B$ in as-quenched state ($S_{as\text{-}q}$) and in deformed state, after HPT (high pressure torsion) deformation ($S_{as\text{-}q\_H}$).

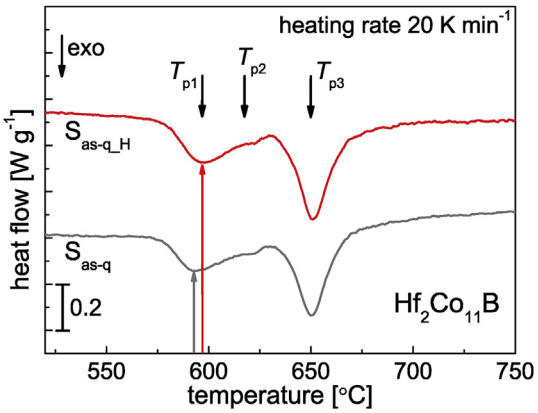

Fig. 2. Differential scanning calorimetry (DSC) curves for $Hf_2Co_{11}B$ in the as-quenched state ($S_{as\text{-}q}$) and after HPT (high pressure torsion) deformation ($S_{as\text{-}qH}$), with the maxima of the first crystallization peak marked by grey and red arrows, respectively. (For interpretation of the references to colour in this figure legend, the reader is referred to the Web version of this article.)

McGuire *et al.* results [17]. The value of saturation magnetization M_s for the as-quenched ribbon is equal to 633 emu cm^{-3} and is lower than that for the deformed sample of $M_s = 679$ emu/cm^{-3}. In both cases the coercive field is very low $H_c < 0.50$ Oe, which is typical of amorphous structure. Slightly improved soft magnetic properties can indicate disappearance of inhomogeneities in the form of nanocrystals or atomic clusters.

The crystalline structure of the annealed sample (Fig. 4) is characteristic of $Hf_2Co_{11}B$ alloy at the early stage of crystallization [21]. The crystallization process is complex and has been described in more details previously [21,26]. The main phases which are formed during first two crystallization steps (marked with T_{p1} and T_{p2} in Fig. 2) are: (i) rhombohedral Hf_2Co_{11}, (ii) orthorhombic Hf_2Co_{11}, and (iii) cubic $Co_{23}B_6$. It is the most important to emphasize the presence of Hf_2Co_{11} rhombohedral phase, which is responsible for hard magnetic properties [21].

The XRD pattern of the deformed sample (S_{AH}) reveals that the partially crystalline sample becomes fully amorphous after HPT. The analysis of the amorphous *halo* indicates small differences in comparison to the as-quenched alloy. The size of coherently scattered domains is equal to 15 Å and the shortest interatomic distance is $R = 2.55$ Å. Subsequent annealing of the deformed sample results in crystallization of rhombohedral and/or orthorhombic Hf_2Co_{11} phase/phases, as the visible peak matches the position of the most intense peak characteristic of both phases. Due to the XRD method limitations it is hard to refine the structure more precisely. Some decisive conclusions concerning the structure are drawn in the following paragraphs on the basis of transmission electron microscopy and magnetic measurements.

Differential scanning calorimetry (DSC) curve for the annealed sample (S_A - Fig. 5) indicates that the first two crystallization stages were completed during isothermal annealing, however, there is also the third crystallization peak which presence suggests the formation of $HfCo_3B_2$ phase [19]. T_{onset} is equal in this case to about 635 °C and $T_p = 652$ °C in accordance with the results presented in Fig. 2 for as-quenched ($S_{as\text{-}q}$) and deformed alloys ($S_{as\text{-}q\_H}$).

The annealed ribbon after HPT (S_{AH}) exhibits X-ray diffraction pattern typical of an amorphous alloy. To confirm it, there should be equivalence between the shapes of DSC curves of $S_{as\text{-}q}$ (Fig. 2) and S_{AH} (Fig. 5). However, it is not the case, as a significantly reduced peak is observed for S_{AH} between 550 and 620 °C. The enthalpy of first two crystallization stages was reduced from 11.17 J g^{-1} for $S_{as\text{-}q}$ to 3.65 J g^{-1} for S_{AH}. It could suggest the presence of nanocrystals embedded in the amorphous matrix, with the volume fraction which is not detectable by X-ray diffraction experiment. Characteristic crystallization temperatures are hard to determine due to the strongly broadened shape (T_{p1} mark is used as a guide only). For the second peak, $T_{onset} = 626$ °C and $T_{p2} = 641$ °C. To sum up, the use of combined HPT/annealing approach is a good way to shift some of the alloys on the free energy scale in both directions with the amorphous state and fully crystalline form as limiting cases.

Transmission electron microscopy (TEM) results gave explicit confirmation of the conclusions drawn on the basis of differential scanning calorimetry, namely indicate the presence of nanocrystallites in the sample after annealing and subsequent HPT (S_{AH}) and its dissimilarity to the as-quenched ribbon ($S_{as\text{-}q}$). Bright field TEM image of $S_{as\text{-}q}$ is presented in Fig. 6a along with the high resolution TEM (b, c) and selected area electron diffraction (d). The results unambiguously corroborate the presence of amorphous structure with trace amounts of small crystallites up to 5 nm in diameter (visible in Fig. 6c).

The long needle-like grains (up to 100 nm in the crosswise direction) embedded in the amorphous matrix are visible in the bright field TEM image (Fig. 7a) of $Hf_2Co_{11}B$ after annealing and subsequent high pressure torsion (S_{AH}). It confirms that the amorphization was not completed during the plastic deformation process. High resolution images (shown in Fig. 7b and c) were acquired from partially crystalline and amorphous regions. SAED pattern from large areas, including crystallized needle shaped

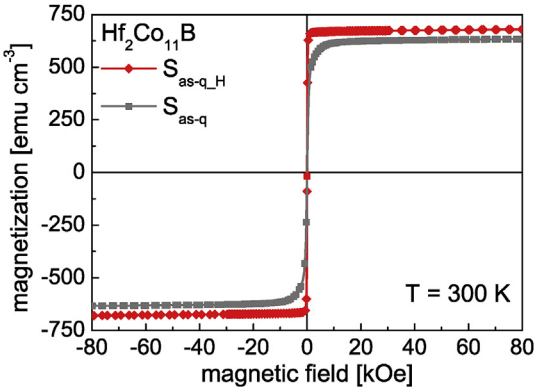

Fig. 3. Magnetic hysteresis loops for $Hf_2Co_{11}B$ in as-quenched state ($S_{as\text{-}q}$) and after HPT (high pressure torsion) ($S_{as\text{-}q\_H}$) measured at room temperature.

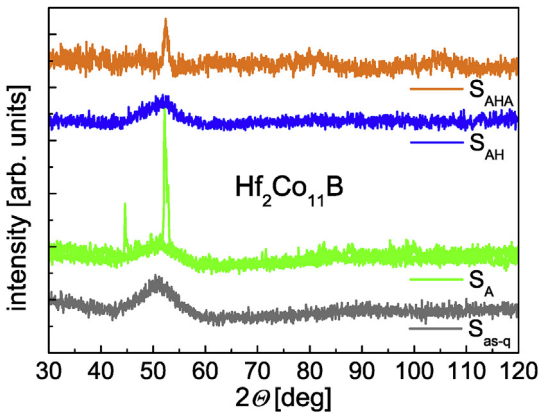

Fig. 4. X-ray diffraction (XRD) patterns of $Hf_2Co_{11}B$ in the succeeding steps of synthesis: as-quenched ($S_{as\text{-}q}$), after isothermal annealing (S_A), after HPT (high pressure torsion) process (S_{AH}) and after second isothermal annealing (S_{AHA}).

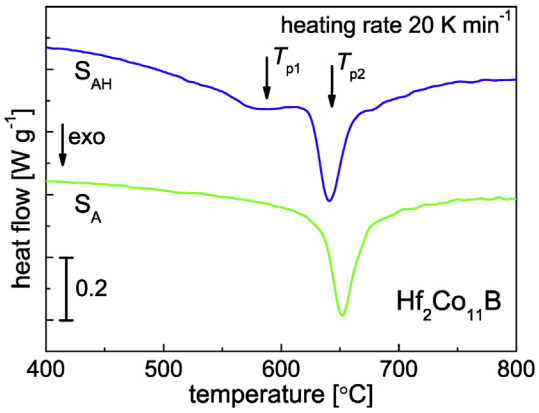

Fig. 5. DSC curves for $Hf_2Co_{11}B$ annealed at $T_a = 570\,^{\circ}C$ for $\tau_a = 60$ min (S_A) and after subsequent HPT (high pressure torsion) process (S_{AH}).

precipitates and the amorphous matrix, showed clearly both sharp diffraction spots and the diffused intensities (Fig. 7d). Because of strong diffuse scattering intensities at low angle, the diffractions corresponding to large lattice spacing are difficult to discern in SAED pattern. However, about 8 Å lattice spacings were clearly revealed by the Fast Fourier Transforms (FFT) of some HRTEM images (shown in the inset of Fig. 7b), suggesting the occurrence of Hf-rich phase (Hf_2Co_{11} or similar μ-phase) [27,28].

M(H) hysteresis loops measured at room temperature are shown in Fig. 8. The curves are exhibited for the samples at each of the synthesis steps: (i) as-quenched ($S_{as\text{-}q}$), (ii) annealed at $T_a = 570\,^{\circ}C$ for $\tau_a = 60$ min (S_A), (iii) after subsequent deformation by HPT (S_{AH}) and finally (iv) after second annealing in the same conditions (S_{AHA}). For a better clarity of the graph, loop for the $S_{as\text{-}q\text{–}H}$ sample was not included (is shown in Fig. 2). The annealing slightly decreases the magnetization M_{80kOe} at magnetic field equal to 80 kOe from 633 to 622 emu cm^{-3} in comparison with as-quenched alloy ($S_{as\text{-}q}$). We do not use a saturation magnetization term, as the curves for annealed samples are not saturated. After deformation, M_{80kOe} is equal to 657 emu cm^{-3}, and similar to the M_s value for the as-quenched state. The second annealing (annealing after deformation) leads to a decrease in M_{80kOe} to 602 emu cm^{-3}. Coercive field H_c, initially increased after annealing from as-quenched state to about 0.7 kOe, then deformation caused its decrease to 0.2 kOe, which is expected due to the amorphization processes. It should be underlined here, that the latter value did not match the coercivity of the as-quenched sample due to the presence of nanocrystals, as confirmed on the basis of DSC and TEM results. The second annealing resulted in renewed increase in H_c, which reached 1.3 kOe. It is almost twice the value for the sample annealed from the as-quenched state (S_A). Embedded nanocrystals play a role of growth facilitators of hard magnetic phase as we have reported for partially crystalline melt-spun ribbon [21]. For this reason the optimization of high pressure torsion parameters and subsequent isothermal annealing conditions are an effective method for improvement of hard magnetic properties of nanocrystalline systems.

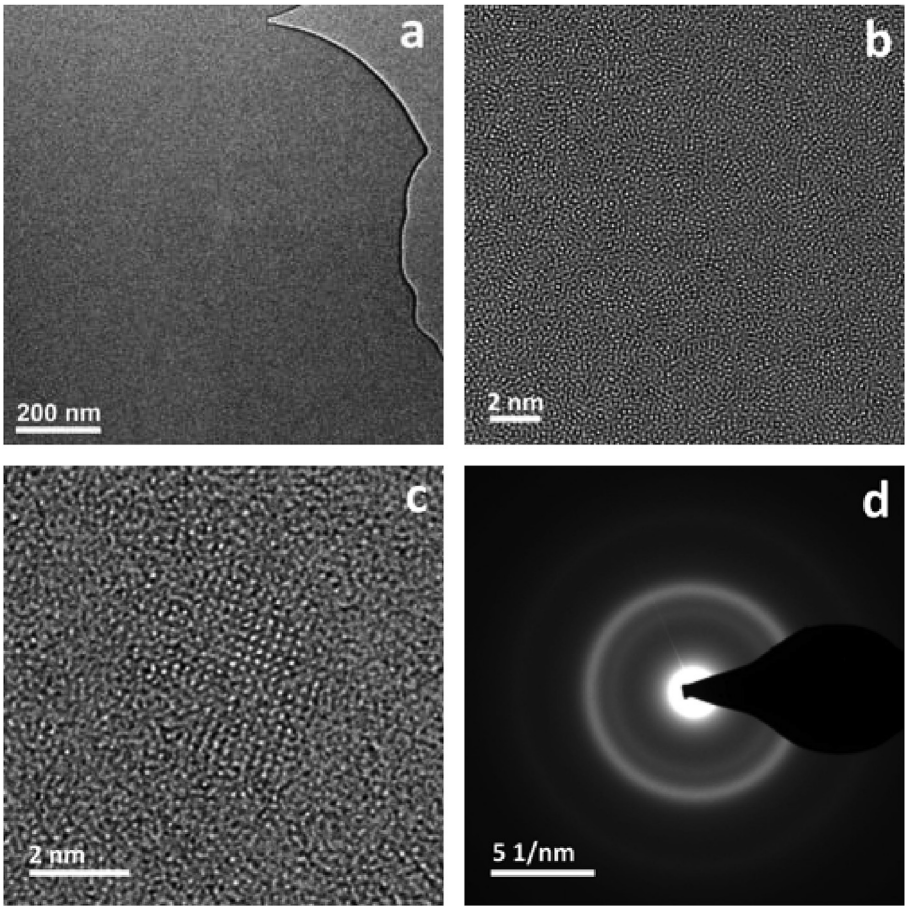

Fig. 6. Bright field TEM (a) and HRTEM (b and c) images along with the selected area electron diffraction (d) of $Hf_2Co_{11}B$ in the as-quenched state ($S_{as\text{-}q}$). (TEM - transmission electron microscopy; HRTEM - high resolution transmission electron microscopy).

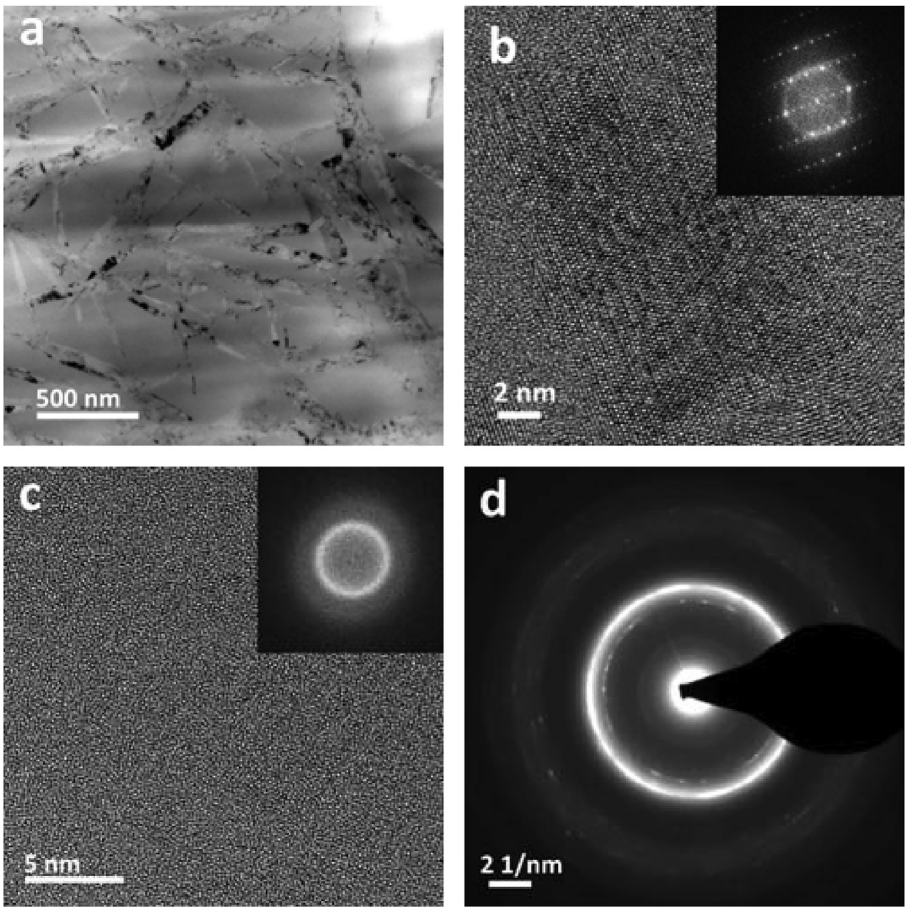

Fig. 7. Bright field TEM (a) and HRTEM (b, c) images along with the selected area electron diffraction (d) of $Hf_2Co_{11}B$ after annealing and subsequent high pressure torsion (HPT) plastic deformation (S_{AH}). Fast Fourier transforms (FFT) are shown in the insets. (TEM - transmission electron microscopy; HRTEM - high resolution transmission electron microscopy).

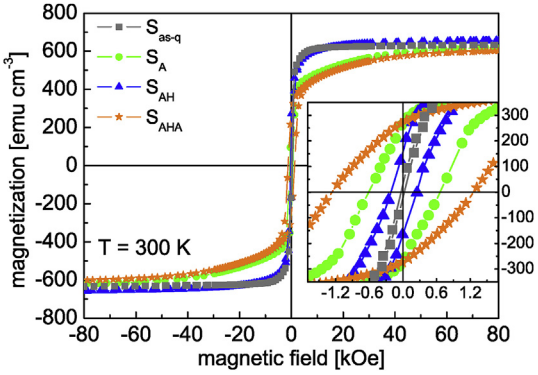

Fig. 8. Magnetic hysteresis loops for $Hf_2Co_{11}B$ in different stages of synthesis: (i) as-quenched ($S_{as\text{-}q}$), (ii) annealed at $T_a = 570\,^{\circ}C$ for $\tau_a = 60$ min (S_A), (iii) HPT (high pressure torsion) deformed (S_{AH}) and (iv) after second annealing at $T_a = 570\,^{\circ}C$ for $\tau_a = 60$ min (S_{AHA}).

High field regions of magnetization curves for the alloy in the as-quenched state ($S_{as\text{-}q}$) after plastic deformation ($S_{as\text{-}q\_H}$), after annealing (S_A), after annealing and deformation (S_{AH}) and at last after additional annealing (S_{AHA}) are shown in Fig. 9. Most of the samples are far from being saturated even in 80 kOe magnetic field, which suggests the presence of highly anisotropic fraction. The law of approach to saturation for magnetization measurements in high magnetic fields was used to calculate the magnetic anisotropy constant K_1 [29]. It also allowed determination of the saturation magnetization M_s for all investigated samples. M_s for the as-quenched sample ($S_{as\text{-}q}$) is equal to about 625 emu cm^{-3} and after HPT ($S_{as\text{-}q\_H}$) it is increased to 671 emu cm^{-3}. The results are consistent with M_s values determined directly from hysteresis loops. It is in accordance with the fact that trace amounts of nanocrystals were embedded in the rapidly quenched alloy, which was confirmed on the basis of HRTEM. Annealing of the as-quenched alloy led to slight decrease in magnetization to 618 emu cm^{-3}. HPT deformation of the annealed ribbon increased magnetization once again, up to 648 emu cm^{-3} and finally the second annealing decreased M_s to 598 emu cm^{-3}. Black curves (Fig. 9) are the best fit lines. The determined magnetic anisotropy constants are equal to 2.23, 1.77, 11.14, 5.03 and 11.07 Merg cm^{-3} for $S_{as\text{-}q}$, $S_{as\text{-}q\_H}$, S_A, S_{AH} and S_{AHA} samples, respectively. The annealing leads to increase in K_1, as shown earlier for Zr-Co and Hf-Co compounds [21,30], and is connected with the formation of rhombohedral Hf_2Co_{11} hard magnetic phase. According to the XRD, TEM results and magnetic measurements, decrease in K_1 after HPT is rather obvious and is triggered by the amorphization. The anisotropy constant values after annealing from amorphous (S_A) and from deformed state after HPT process (S_{AHA}) are the same within the calculation error. The obtained values are comparable to those presented by Balasubramanian *et al.* for Hf-Co nanoparticles [31].

Largely reversible demagnetization in conjunction with a magnetic remanence ratio m_r, defined as M_r/M_s, can be used as a criterion describing exchange interaction between magnetic phases,

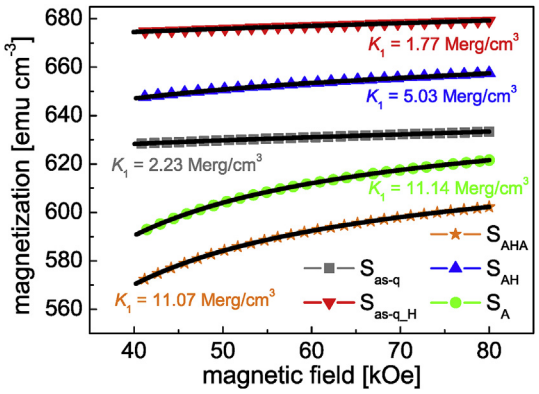

Fig. 9. Magnetic field dependence of magnetization (40–80 kOe), measured at 300 K for $Hf_2Co_{11}B$ alloys in different stages of synthesis: (i) as-quenched (S_{as-q}), (ii) annealed at $T_a = 570\,^{\circ}C$ for $\tau_a = 60$ min (S_A), (iii) annealed sample after HPT (high pressure torsion) (S_{AH}) and (iv) after second annealing at $T_a = 570\,^{\circ}C$ for $\tau_a = 60$ min (S_{AHA}), (v) as-quenched sample after HPT (S_{as-q_H}).

where $m_r > 0.5$ indicates that magnetic phases are exchange coupled [32]. The calculated values are equal to 0.43, 0.25 and 0.45 for S_A, S_{AH} and S_{AHA}, respectively, neglecting the coupling in all of the investigated alloys. It can be confirmed also on the basis of *dM/dH vs. H* graphs, which are presented in Fig. 10. For the as-quenched sample one peak is visible in the vicinity of zero field, and originated from the amorphous phase. For the as-quenched sample subjected to HPT process the peak at zero field is narrower in comparison to the as-quenched ribbon, as the amorphous structure is more uniform and we do not expect the presence of any structural imperfections. One can see the broad peak with the maximum at around 1 kOe and small zero field kink after annealing. The broad peak in higher field can be deconvoluted to two peaks, originating from the mixture of two different magnetic phases. The volume fraction of non-soft magnetic phases is decreased for the S_{AH} as there are just two small inflections at negative field shoulder of d*M*/d*H vs. H* peak. This is another evidence for the presence of Hf_2Co_{11} nanocrystals in the deformed sample and is in line with enhanced $K_1 = 5.03$ Merg cm^{-3} (in comparison to S_{as-q}) and with the results of DSC and TEM analysis. Large peak connected with the soft magnetic matrix is dominant again. Annealing of deformed sample resulted in the formation of the very broad peak with more intense hard magnetic component. Further improvement in the synthesis parameters should result in the optimization of volume fractions and grain sizes of soft and hard magnetic phases and the onset of exchange coupling, consequently followed by the increase of coercivity and saturation magnetization [33,34].

Magnetic anisotropy constant K_1 *versus* magnetic polarization J_s is plotted in Fig. 11 with highlighted magnetic hardness factor lines κ. The κ value is described as $\kappa = (\mu_0 K_1/(J_s^2))^{1/2}$ [35]. The materials for permanent magnet applications should be characterized by κ higher than 1. For $Hf_2Co_{11}B$ alloys this criterion is fulfilled. The obtained values are similar to those of Mn-based alloys, higher comparing to MnBi, but slightly lower than κ for MnAl alloy. Large spin-orbit coupling characteristic of the 5*d*-element results in the highest magnetic anisotropy for the FePt alloy ($L1_0$ phase) and its high κ value. FePt compound has lower saturation magnetization in comparison to $Nd_2Fe_{14}B$ alloy. The $Nd_2Fe_{14}B$ alloy possess high κ, K_1 and saturation magnetization. Generally, high magnetic anisotropy is typical of rare-earth-based compounds, originating mainly from the strong spin-orbit coupling of the rare-earth 4*f* electrons and resulting in the high values of *K* for Nd-Fe-B, Dy-Fe-B, Sm-Fe or Sm-Co [38].

4. Conclusion

We have reported an innovative approach to isolate the Hf_2Co_{11} phase by special preparation conditions (melt-spinning, high pressure torsion and specific heat treatment). This approach has significantly increased the understanding of the properties of this phase and its impact on magnetic performance. The thermal stability and magnetic properties of $Hf_2Co_{11}B$ amorphous and partially crystalline ribbons in the as-quenched state, after severe plastic deformation by high pressure torsion and subsequent annealing, were analyzed and discussed. The HPT deformation slightly improved thermal stability and soft magnetic properties of the ribbon due to the disappearance of nanocrystals, which existed in trace amounts in the rapidly quenched sample. Furthermore, starting from partially crystalline $Hf_2Co_{11}B$ alloy, the HPT process led to the amorphization, although the coexistence of small needle-like nanocrystals (not visible in XRD) was confirmed by TEM. Isothermal annealing of $Hf_2Co_{11}B$ ribbon after HPT processing resulted in a higher coercive field, in comparison to that of the as-quenched sample after annealing in the same conditions. Another confirmation of our conclusion is that the presence of the embedded nanocrystals of the hard magnetic Hf_2Co_{11} phase, as documented by TEM analysis, improved magnetic properties of the material studied after isothermal annealing. This shows that severe

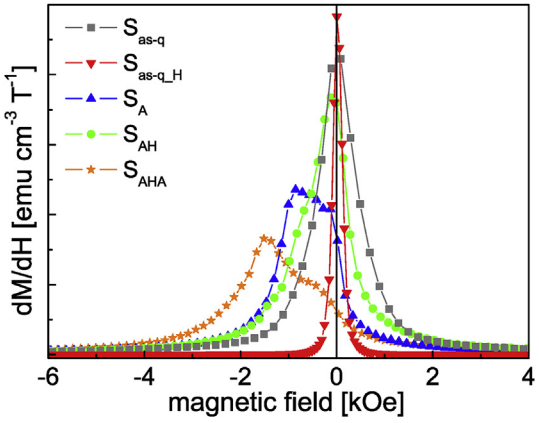

Fig. 10. The *dM/dH vs. H* curves for $Hf_2Co_{11}B$ alloys in different stages: (i) as-quenched (S_{as-q}), (ii) annealed at $T_a = 570\,^{\circ}C$ for $\tau_a = 60$ min (S_A), (iii) annealed sample after HPT (high pressure torsion) plastic deformation (S_{AH}) and (iv) after second annealing at $T_a = 570\,^{\circ}C$ for $\tau_a = 60$ min (S_{AHA}), (v) as-quenched sample after HPT (S_{as-q_H}).

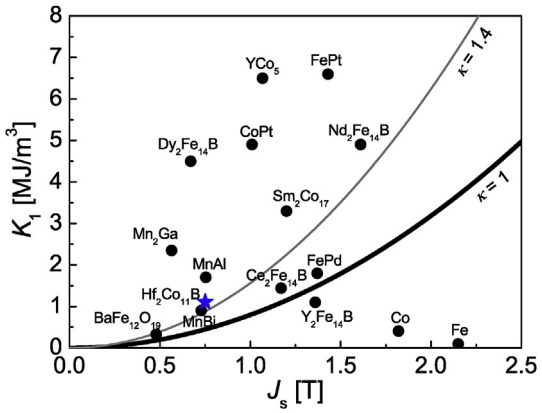

Fig. 11. Magnetic anisotropy constant K_1 *vs.* magnetic polarization J_s dependence for different magnetic systems with solid lines representing characteristic κ (magnetic hardness factor) values [35–37].

plastic deformation and heat treatment allows tuning of the structural and magnetic properties in initially amorphous magnetic materials, which have already been comparable to that of the other rare-earth free permanent magnets.

Acknowledgments

The authors gratefully acknowledge the financial support of the National Science Centre (Project No. 2016/23/N/ST3/03820) and of DAAD/MNiSW Project Based Personal Exchange Program (PPP) in years 2016–2017.

References

[1] M. Rajasekhar, D. Akhtar, M.M. Raja, S. Ram, V. Chandrasekaran, J. Phys. D Appl. Phys. 42 (2009), 095009.
[2] A. Pasko, F. Mazaleyrat, M. LoBue, E. Fazakas, L.K. Varga, EPJ Web Conf. 40 (2013) 06008.
[3] T. Saito, R. Nishimura, D. Nishio-Hamane, J. Magn. Magn. Mater. 349 (2014) 9–14.
[4] Y. Jin, W. Zhang, P.R. Kharel, S.R. Valloppilly, R. Skomski, D.J. Sellmyer, AIP Adv. 6 (2016), 056002.
[5] M. Kopcewicz, A. Grabias, I. Škorvánek, J. Marcin, B. Idzikowski, J. Appl. Phys. 85 (1999) 4427–4429.
[6] M. Miglierini, I. Tóth, M. Seberíni, E. Illeková, B. Idzikowski, J. Phys. Condens. Matter 14 (2002) 1249–1260.
[7] E. Dorolti, A.V. Trifu, O. Isnard, I. Chicinaş, F. Tolea, M. Valeanu, V. Pop, J. Alloys Compd. 560 (2013) 189–194.
[8] J.Z. Wei, Z.G. Song, Y.B. Yang, S.Q. Liu, H.L. Du, J.Z. Han, D. Zhou, C.S. Wang, Y.C. Yang, A. Franz, D. Többens, J.B. Yang, AIP Adv. 4 (2014) 127113.
[9] H.W. Chang, C.F. Tsai, C.C. Hsieh, C.W. Shih, W.C. Chang, C.C. Shaw, J. Magn. Magn. Mater. 346 (2013) 74–77.
[10] T.G. Woodcock, F. Bittner, T. Mix, K.-H. Müller, S. Sawatzki, O. Gutfleisch, J. Magn. Magn. Mater. 360 (2014) 157–164.
[11] N. Tang, Z. Chen, Y. Zhang, G.C. Hadjipanayis, F. Yang, J. Magn. Magn. Mater. 219 (2000) 173–177.
[12] R.Z. Valiev, A.V. Korznikov, R.R. Mulyukov, Mater. Sci. Eng. A 168 (1993) 141–148.
[13] R.Z. Valiev, R.K. Islamgaliev, I.V. Alexandrov, Prog. Mater. Sci. 45 (2000) 103–189.
[14] B. Straumal, A. Korneva, P. Zieba, Arch. Civ. Mech. Eng. 14 (2014) 242–249.
[15] R.V. Sundeev, A.M. Glezer, A.V. Shalimova, J. Alloys Compd. 611 (2014) 292–296.
[16] R.V. Sundeev, A.M. Glezer, A.V. Shalimova, Mater. Lett. 133 (2014) 32–34.
[17] M.A. McGuire, O. Rios, N.J. Ghimire, M. Koehler, Appl. Phys. Lett. 101 (2012), 202401.
[18] B. Das, B. Balamurugan, P. Kumar, R. Skomski, V.R. Shah, J.E. Shield, A. Kashyap, D.J. Sellmyer, IEEE Trans. Magn. 49 (2013) 3330–3333.
[19] W.Y. Zhang, X.Z. Li, S. Valloppilly, R. Skomski, J.E. Shield, A. Kashyap, D.J. Sellmyer, J. Phys. D. Appl. Phys. 46 (2013), 135004.
[20] M.A. McGuire, O. Rios, J. Appl. Phys. 117 (2015) 53912.
[21] A. Musiał, Z. Śniadecki, J. Marcin, J. Kováč, I. Škorvánek, B. Idzikowski, J. Alloys Compd. 665 (2016) 93–99.
[22] A. Guinier, X-Ray Diffraction in Crystals, Imperfect Crystals and Amorphous Bodies, San Francisco, 1963.
[23] Z. Śniadecki, J. Marcin, I. Škorvánek, N. Pierunek, B. Idzikowski, J. Alloys Compd. 584 (2014) 477–482.
[24] A. Inoue, H. Koshiba, T. Itoi, A. Makino, Appl. Phys. Lett. 73 (1998) 744–746.
[25] Y. Du, Y. Kan, X. Lu, Y. Liu, H. Bo, W. Cai, D. Hu, F. Huang, J. Zhu, Phys. Status Solidi Rapid Res. Lett. 7 (2013) 506–509.
[26] A. Musiał, Z. Śniadecki, B. Idzikowski, Mater. Des. 114 (2016) 404–409.
[27] X.Z. Li, Y.L. Jin, M.Y. Wang, J.E. Shield, R. Skomski, D.J. Sellmyer, Intermetallics 75 (2016) 54–61.
[28] X. Lu, K. Cheng, S. Liu, K. Li, F. Zheng, Y. Du, J. Alloys Compd. 627 (2015) 251–260.
[29] G. Hadjipanayis, D.J. Sellmyer, B. Brandt, Phys. Rev. B 23 (1981) 3349–3354.
[30] W.Y. Zhang, X.Z. Li, S. Valloppilly, R. Skomski, D.J. Sellmyer, Mater. Sci. Eng. A 186 (2014) 64–67.
[31] B. Balasubramanian, P. Mukherjee, R. Skomski, P. Manchanda, B. Das, D.J. Sellmyer, Sci. Rep. 4 (2014) 6265.
[32] E.F. Kneller, R. Hawig, IEEE Trans. Magn. 27 (1991) 3588–3600.
[33] M. Szwaja, P. Gębara, J. Filipecki, K. Pawlik, A. Przybył, P. Pawlik, J.J. Wysłocki, K. Filipecka, J. Magn. Magn. Mater. 382 (2015) 307–311.
[34] A. Przybył, K. Pawlik, P. Pawlik, P. Gębara, J.J. Wysłocki, J. Alloys Compd. 536 (2012) 333–336.
[35] J.M.D. Coey, Magnetism and Magnetic Materials, Cambridge University Press, Cambridge, 2010.
[36] M. Sagawa, S. Hirosawa, H. Yamamoto, S. Fujimura, Y. Matsuura, Jpn. J. Appl. Phys. 26 (1987) 785–800.
[37] D.J. Sellmyer, R. Skomski, Advanced Magnetic Nanostructures, Springer, New York, 2006.
[38] S. Hirosawa, J. Magn. Soc. Jpn. 39 (2015) 85–95.